Synthetic phase-shifting for optical testing: Point-diffraction interferometry without null optics or phase shifters

Ryeojin Park,[1,3,*] Dae Wook Kim,[1] and Harrison H. Barrett[1,2,3]

[1]College of Optical Sciences, University of Arizona, Tucson, Arizona 85721, USA
[2]Department of Medical Imaging, University of Arizona, Tucson, Arizona 85721, USA
[3]Center for Gamma-Ray Imaging, University of Arizona, Tucson, Arizona 85721, USA
[*]rpark@optics.arizona.edu

Abstract: An innovative iterative search method called the synthetic phase-shifting (SPS) algorithm is proposed. This search algorithm is used for maximum-likelihood (ML) estimation of a wavefront that is described by a finite set of Zernike Fringe polynomials. In this paper, we estimate the coefficient, or parameter, values of the wavefront using a single interferogram obtained from a point-diffraction interferometer (PDI). In order to find the estimates, we first calculate the squared-difference between the measured and simulated interferograms. Under certain assumptions, this squared-difference image can be treated as an interferogram showing the phase difference between the true wavefront deviation and simulated wavefront deviation. The wavefront deviation is the difference between the reference and the test wavefronts. We calculate the phase difference using a traditional phase-shifting technique without physical phase-shifters. We present a detailed forward model for the PDI interferogram, including the effect of the finite size of a detector pixel. The algorithm was validated with computational studies and its performance and constraints are discussed. A prototype PDI was built and the algorithm was also experimentally validated. A large wavefront deviation was successfully estimated without using null optics or physical phase-shifters. The experimental result shows that the proposed algorithm has great potential to provide an accurate tool for non-null testing.

References and links

1. V. Genberg, G. Michels, and K. B. Doyle, "Orthogonality of Zernike polynomials," Proc. SPIE **4771**, 276–286 (2002).
2. D. Malacara, *Optical Shop Testing* (Wiley, 1978).
3. J. E. Greivenkamp and R. O. Gappinger, "Design of a nonnull interferometer for aspheric wave fronts," Appl. Opt. **43**(27), 5143–5151 (2004).
4. J. E. Greivenkamp, "Sub-Nyquist interferometry," Appl. Opt. **26**(24), 5245–5258 (1987).
5. J. E. Greivenkamp, A. E. Lowman, and R. J. Palum, "Sub-Nyquist interferometry: implementation and measurement capability," Opt. Eng. **35**(10), 2962–2969 (1996).
6. H. H. Barrett and K. J. Myers, *Foundations of Image Science* (Wiley, 2004).
7. H. H. Barrett, C. Dainty, and D. Lara, "Maximum-likelihood methods in wavefront sensing: stochastic models and likelihood functions," J. Opt. Soc. Am. A **24**(2), 391–414 (2007).
8. J. A. Sakamoto and H. H. Barrett, "Maximum-likelihood estimation of parameterized wavefronts from multifocal data," Opt. Express **20**(14), 15928–15944 (2012).
9. J. A. Sakamoto, H. H. Barrett, and A. V. Goncharov, "Inverse optical design of the human eye using likelihood methods and wavefront sensing," Opt. Express **16**(1), 304–314 (2008).
10. W. P. Linnik, "A simple interferometer for the investigation of optical systems," C. R. Acad. Sci. URSS **5**, 208–210 (1933).

11. R. N. Smartt and W. H. Steel, "Theory and Application of Point-Diffraction Interferometers," Jpn. J. Appl. Phys. **14**, 351–356 (1975).
12. R. M. Goldstein, H. A. Zebker, and C. L. Werner, "Satellite radar interferometry: Two-dimensional phase unwrapping," Radio Sci. **23**(4), 713–720 (1988).
13. D. Ruijters, B. M. ter Harr Romeny, and P. Suetens, "Efficient GPU-accelerated elastic image registration," in *Proceedings Sixth IASTED international conference on biomedical engineering* (BioMed), pp. 419–424 (2008).
14. G. E. Sommargren, "Phase shifting diffraction interferometry for measuring extreme ultraviolet optics," No. UCRL-JC–123549, CONF-9604150–1, Lawrence Livermore National Lab., CA (1996).
15. C. R. Mercer and K. Creath, "Liquid-crystal point-diffraction interferometer for wave-front measurements," Appl. Opt. **35**(10), 1633–1642 (1996).
16. R. M. Neal and J. C. Wyant, "Polarization phase-shifting point-diffraction interferometer," Appl. Opt. **45**(15), 3463–3476 (2006).
17. M. Paturzo, F. Pignatiello, S. Grilli, S. De Nicola, and P. Ferraro, "Phase-shifting point-diffraction interferometer developed by using the electro-optic effect in ferroelectric crystals," Opt. Lett. **31**(24), 3597–3599 (2006).
18. J. E. Millerd, N. J. Brock, J. B. Hayes, and J. C. Wyant, "Instantaneous phase-shift point-diffraction interferometer," Proc. SPIE **5531**, 264–272 (2004).
19. P. Su, J. Burge, R. A. Sprowl, and J. Sasian,"Maximum likelihood estimation as a general method of combining subaperture data for interferometric testing," Proc. SPIE **6342**, 1X–1X-6 (2006).

1. Introduction

In optical metrology, interferometry is widely used in order to infer physical quantities of interest from an interferogram. Depending on the task, the physical quantities can be aberration coefficients, refractive-index gradient distribution, surface deformation, or alignment errors. The task of our work is to estimate the coefficient values of a test wavefront, expanded in a finite set of Zernike Fringe [ZF] polynomials [1], from a single interferogram.

The continuous irradiance pattern in an interferogram is given by the well-known expression,

$$I(x, y) = I_1 + I_2 + 2\sqrt{I_1 I_2} \cos[\phi_{test} - \phi_{ref}], \qquad (1)$$

where I_1 and I_2 are the irradiance of the test and reference beam, and $\phi_{test} - \phi_{ref}$ is the phase difference between the test and reference beams. The irradiance pattern is often detected by a digital detector which integrates the irradiance over each pixel in an array. It is usually assumed that the detector simply samples the interferogram at a discrete set of points. However, when measuring a strong asphericity or a large aberration of a test optic, the spatial fringe period is often significantly smaller than the area of one pixel. The integration over a pixel then blurs out the fine structure in the interferogram instead of merely sampling it. Both the blurring by the pixel and the sampling reduce the ability to perform the task for which the interferogram was intended. To avoid this issue, most interferometry is used in a null configuration [2]. Null optics can compensate for a large aberration of a test optic such that the absolute value of the wavefront difference between any two adjacent pixels is less than half a wave, which is the well-known Nyquist condition [3]. The main disadvantage of using null optics is that a particular null optic has to be designed for the specific test optic, which increases the cost of the system and the production time. In order to overcome these limitations, Sub-Nyquist interferometry (SNI) was developed [3–5]. As a phase-shifting approach, SNI achieves a high dynamic range by recovering the phase information from the subsampled interferogram (by a sparse sensor) assuming the wavefront or surface slope is continuous.

Unlike SNI, we extract the phase information from a single interferogram obtained from a contiguous detector with a finite pixel size. For this approach, we estimate the ZF coefficients of the test wavefront, described by a finite set of ZF polynomials, via maximum-likelihood (ML) estimation. The advantages of the statistical approach in imaging are well understood [6]. ML estimation in wavefront sensing has been rigorously discussed by Barrett et al. [7] and ML estimation of parameterized wavefronts from multifocal data has been developed

using simulated annealing, a global optimization algorithm [8]. Despite its advantages, the limitation of search algorithms for ML estimation in a high-dimensional parameter space, such as ZF coefficient space, is the computational time. A fast conjugate-gradient method can be applied if the likelihood is monotonic even in high-dimensional parameter space. However, if the likelihood surface has many local minima and strong coupling between parameters, time-consuming global optimization is often the only choice [8,9]. To overcome this challenge, the innovative iterative search algorithm, called the synthetic phase-shifting (SPS) algorithm is developed. The SPS algorithm is far less computationally expensive than global search algorithms such as simulated annealing.

The SPS algorithm iteratively finds the coefficient values that minimize the squared difference between a single measured interferogram and an accurate computer-simulated interferogram. This approach becomes ML estimation if the random errors between the measured and simulated interferograms follow an independent and identically distributed normal distribution [6,7]. Based on an accurate forward model, a simulated interferogram is generated with a test wavefront, expanded by the nominal coefficient values, and a known reference wavefront. We then calculate the squared-difference image between the measured and simulated interferograms. We show that, under certain constraints, this squared-difference image can be recognized as an interferogram which shows the phase difference between the true wavefront deviation and simulated wavefront deviation. The wavefront deviation is the difference between the reference and the test wavefronts. We apply a traditional phase-shifting method to extract the phase difference. By adding the result of the unwrapped phase, the coefficient values of the test wavefront are updated. These updated coefficient values are used as the nominal coefficient values for the next iteration. Note that the algorithm utilizes traditional phase-shifting techniques, but it does not require any physical phase-shifters. To our knowledge, ML estimation of parameterized wavefront using the SPS algorithm is the first static interferometric technique applied to data which do not satisfy the Nyquist condition.

In this paper, we established the theory of the SPS algorithm, validated it with computer simulations, and discussed its advantages and limitations. We have built a proof-of-concept prototype point-diffraction interferometer (PDI). An experimentally measured interferogram from the PDI was used to verify the practical applicability of the algorithm. The results show that the proposed algorithm has great potential for non-null testing and can achieve high measurement accuracy without using physical phase-shifters.

2. Theory

2.1 Maximum-likelihood estimation

In this study, a single interferogram is the raw CCD output from the PDI. The principle of the PDI is simple [10,11]. Illumination light passes through a test lens and focuses onto a PDI plate, a neutral density filter with a clear pinhole in the center. When the focused beam transmits through the PDI plate, a reference beam is generated by the light diffraction from the pinhole. Simultaneously, the test beam is attenuated by the PDI plate and interferes with the reference beam (Fig. 1). This interference pattern forms an interferogram, g, in which the phase information of the test lens at the detector plane is encoded. The vector, g, is the $M \times 1$ vector of random data from the CCD, and the total number of CCD pixels in the circular aperture is M. Our goal is to extract the test wavefront information from g using ML estimation of the test wavefront, expanded in a finite set of ZF polynomials.
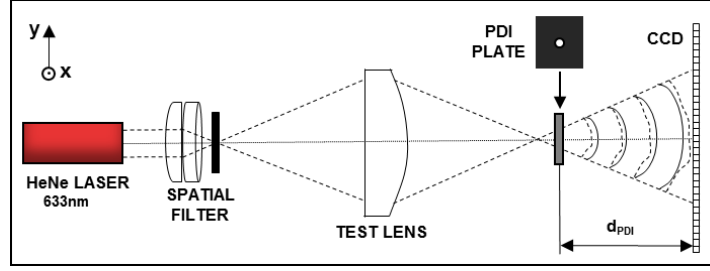
Fig. 1. The schematic of the PDI for non-null testing. Unlike a conventional PDI, physical phase-shifters are not required. The dashed line represents the test beam and its wavefront, and the solid line represents the reference wavefront generated by pinhole diffraction at the PDI plate.

The CCD is assumed to be a discrete array of individual detector elements with no electronic coupling from one element to another, and each element is identical. We assume that the PDI noise follows Gaussian statistics, so the data vector, **g**, follows a probability density function (PDF) denoted by

$$\text{pr}(\mathbf{g}\,|\,\boldsymbol{\theta}) = \prod_{m=1}^{M} \frac{1}{\sqrt{2\pi\sigma_m^{\;2}}} \exp\left\{ -\frac{[g_m - \overline{g}_m(\boldsymbol{\theta})]^2}{2\sigma_m^{\;2}} \right\}, \tag{2}$$

where $\boldsymbol{\theta}$ is 37×1 column vector of the ZF coefficients, g_m is the measured CCD output in the mth pixel, $\overline{g}_m(\boldsymbol{\theta})$ is a mean value of the mth pixel evaluated at $\boldsymbol{\theta}$, and $\sigma_m^{\;2}$ is the variance in each detector element [7]. In general, this variance can depend on illumination level, but for simplicity in what follows, we assume that the variance is the same for all elements, $\sigma_m^{\;2} = \sigma^2$. Since the noise is zero-mean, $\overline{g}_m(\boldsymbol{\theta})$ can be determined by an accurate, noise-free forward model as described in Appendix 7.1. The PDF of the data, $\text{pr}(\mathbf{g}\,|\,\boldsymbol{\theta})$, given the parameters, is also called the likelihood of the parameters given the data. The objective of ML estimation is to find the estimates of $\boldsymbol{\theta}$ that maximize the likelihood.

$$\hat{\boldsymbol{\theta}}_{ML} \equiv \arg\max_{\boldsymbol{\theta}} \text{pr}(\mathbf{g}\,|\,\boldsymbol{\theta}), \tag{3}$$

where $\arg\max$ operator returns the parameter value at which the function is maximized. Since the logarithm is a monotonic transformation, Eq. (3) becomes

$$\hat{\boldsymbol{\theta}}_{ML} \equiv \arg\min_{\boldsymbol{\theta}} \sum_{m=1}^{M} [g_m - \overline{g}_m(\boldsymbol{\theta})]^2, \tag{4}$$

where $\arg\min$ operator returns the parameter value at which the function is minimized. Therefore, analysis of an interferogram reduces to nonlinear least-squares regression between the interferogram and simulated interferogram.

2.2 The synthetic phase-shifting algorithm

Conventional search algorithms for $\hat{\boldsymbol{\theta}}_{ML}$ are computationally expensive, not only because of the high-dimensional parameter space, but also because of the complicated likelihood function. To overcome this challenge, we propose an innovative iterative search algorithm called the SPS algorithm. For this algorithm, we focus on the squared-difference image between a single measured interferogram and an accurate computer simulated interferogram, which is an $M\times1$ vector, denoted $\Delta\mathbf{g}^2$, with its mth component given by

$$\Delta g_m^2 \equiv \left[g_m - \overline{g}_m(\boldsymbol{\theta}) \right]^2. \tag{5}$$

Under certain assumptions, discussed here and in greater detail in Appendix 7.2, we find

$$\Delta g_m^2 \propto \cos\left[2\pi \phi_{diff}(\mathbf{r}_m) \right], \tag{6}$$

where the difference of the wavefront deviations is denoted by

$$\phi_{diff}(\mathbf{r}) = \left[\phi_{test}(\mathbf{r}) - \phi_{ref}(\mathbf{r}) \right] - \left[\hat{\phi}_{test}(\mathbf{r}\,|\,\boldsymbol{\theta}) - \hat{\phi}_{ref}(\mathbf{r}) \right] = \phi_{exp}(\mathbf{r}) - \phi_{sim}(\mathbf{r}). \tag{7}$$

The true wavefront deviation is $\phi_{exp}(\mathbf{r}) = \phi_{test}(\mathbf{r}) - \phi_{ref}(\mathbf{r})$, and the simulated wavefront deviation is $\phi_{sim}(\mathbf{r}\,|\,\boldsymbol{\theta}) = \hat{\phi}_{test}(\mathbf{r}\,|\,\boldsymbol{\theta}) - \hat{\phi}_{ref}(\mathbf{r})$, where the test and reference wavefronts are denoted by $\phi_{test}(\mathbf{r})$ and $\phi_{ref}(\mathbf{r})$, respectively; the corresponding simulated wavefronts are $\hat{\phi}_{test}(\mathbf{r}\,|\,\boldsymbol{\theta})$ and $\hat{\phi}_{ref}(\mathbf{r})$.

The first assumption is that a CCD pixel is small compared to the spatial fringe period of $\phi_{diff}(\mathbf{r})$, so the irradiance fluctuation due to $\phi_{diff}(\mathbf{r})$ is constant over a pixel. This is a much less stringent assumption than requiring that the actual interferogram irradiance be constant over a pixel, which is the usual implicit assumption in interferometry. The squared-difference images in Figs. 2(f)–2(i) show the slowly varying $\phi_{diff}(\mathbf{r})$ over a pixel. With our assumption, therefore, we can simply sample the irradiance fluctuation due to $\phi_{diff}(\mathbf{r})$ at the center position of a CCD pixel instead of integrating over the pixel. The spatial frequency of $\phi_{diff}(\mathbf{r})$ should at least satisfy the Nyquist condition to recover the phase information of $\phi_{diff}(\mathbf{r})$. On the other hand, the second assumption is that the spatial frequency of $\phi_{sum}(\mathbf{r}) = \phi_{exp}(\mathbf{r}) + \phi_{sim}(\mathbf{r})$ should be well beyond the Nyquist frequency, so the fine structure of the irradiance fluctuation due to $\phi_{sum}(\mathbf{r})$ is blurred out by the integration over the pixel (Appendix 7.2). The third assumption is that measured and the simulated mean irradiances are approximately equal.
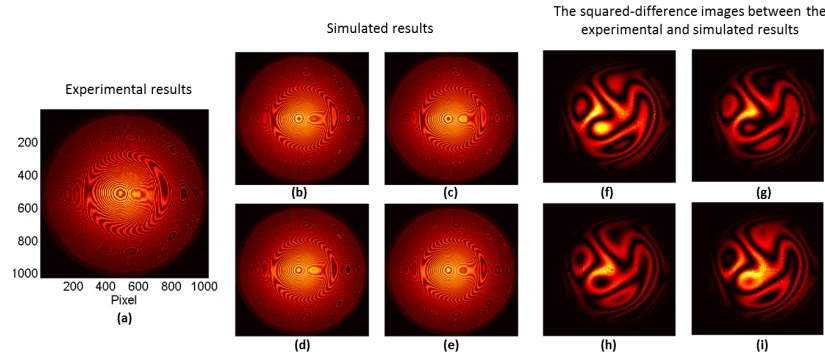
Fig. 2. Graphical demonstration of the synthetic four-step phase-shifting algorithm. (a) The experimental result was generated with the true parameter values based on the forward model, including noise. (b)-(e) The simulated interferograms, without noise, with nominal parameter values at phase-steps $0, \pi/2, \pi, 3\pi/2$. (f)-(i) The squared-difference images between (a) and (b)-(e) respectively. The squared-difference images show the slowly varying $\phi_{diff}(\mathbf{r})$. (Note: some spurious fringes may also be visible due to the aliasing by the monitor display sampling.)

A graphical demonstration of the SPS algorithm is shown in Fig. 2. The SPS algorithm calculates $\phi_{diff}(\mathbf{r}_m)$ using a traditional four-step phase-shifting technique. First, four simulated interferograms are generated at different piston values of the test wavefront. The phase-stepping size between each simulated interferogram is $\pi/2$. From a single measured interferogram, we subtract each phase-shifted simulation result to get the four phase-shifted squared-difference images. After obtaining the wrapped phase map of $\phi_{diff}(\mathbf{r}_m)$, Goldstein's branch-cut phase-unwrapping algorithm [12] is applied. In this study, the residual modeling error for the reference wavefront, $\Delta\hat{\phi}_{ref}(\mathbf{r}_m) = \phi_{ref}(\mathbf{r}_m) - \hat{\phi}_{ref}(\mathbf{r}_m)$, is integrated into the simulated test wavefront. Therefore, the simulated test wavefront is rewritten as $\hat{\phi}_{test}(\mathbf{r}_m \mid \boldsymbol{\theta}) \equiv \hat{\phi}_{test}(\mathbf{r}_m \mid \boldsymbol{\theta}) + \Delta\hat{\phi}_{ref}(\mathbf{r}_m)$. For an ideal case, we know the reference wavefront exactly, so $\Delta\hat{\phi}_{ref}(\mathbf{r}_m \mid \boldsymbol{\theta}_n) = 0$. The true test wavefront at the detector is

$$\phi_{test}(\mathbf{r}_m) \approx \hat{\phi}_{test}(\mathbf{r}_m \mid \boldsymbol{\theta}) + \phi_{diff}(\mathbf{r}_m). \tag{8}$$

Note that the algorithm utilizes the traditional phase-shifting technique, but entirely in the computer; it does not require any physical phase-shifters.

2.3 The iterative process of the synthetic phase-shifting algorithm

Since the SPS algorithm is a search method for the nonlinear least squares regression, we propose an iterative process in order to increase the accuracy of the estimation. Because of the first assumption in Subsection 2.2, we assume that the resulting sampled unwrapped-phase map is continuous and is well approximated by 37 ZF polynomials. At each iteration, j, the ZF coefficients of the unwrapped-phase, $\boldsymbol{\theta}_{diff}^{j}$, are obtained by their orthonormality. At the jth iteration of the SPS algorithm, the nominal ZF coefficient vector of the test wavefront is $\hat{\boldsymbol{\theta}}^{j}$. This coefficient vector is updated by adding $\boldsymbol{\theta}_{diff}^{j}$:

$$\hat{\boldsymbol{\theta}}^{j+1} = \hat{\boldsymbol{\theta}}^{j} + \boldsymbol{\theta}_{diff}^{j}. \tag{9}$$
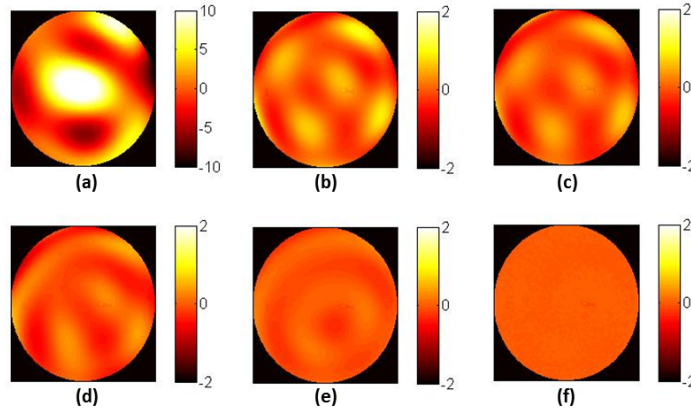
Fig. 3. The unwrapped-phase results after (a) 1, (b) 3, (c) 5, (d) 7, (e) 16, and (f) 25 iterations of the synthetic phase-shifting algorithm. The scale bars are in units of waves.

Figure 3 shows the unwrapping results at different iterations. As iterations increase, the unwrapping map becomes null (i.e. showing only a constant piston-term difference), indicating the estimated test wavefront converges to the true test wavefront. The iterative process is summarized in the flow chart shown in Fig. 4. The box-averaging filtering (post-

filtering of Δg^2) process is optional for noise suppression, but it may improve the convergence rate to the true values. Future work is required to optimize the post-filtering algorithm.

```
                              ( Start )
                                  |
                                  v
+--------------------------------------------------------------+
| Generate the forward model, g̅(θ̂¹), using the initial         |
| nominal values from ZEMAX.                                    |
+--------------------------------------------------------------+
                                  |
                                  v
+--------------------------------------------------------------+
| Calculate the square-difference between the measured and     |
| the simulated interferograms, Δg².                           |
+--------------------------------------------------------------+
                                  |
                                  v
+--------------------------------------------------------------+
| Apply box-averaging filtering to Δg².                        |
+--------------------------------------------------------------+
                                  |
                                  v
+--------------------------------------------------------------+
| Apply the synthetic phase-shifting algorithm to the result.  |
+--------------------------------------------------------------+
                                  |
                                  v
+--------------------------------------------------------------+
| Apply Goldstein's phase unwrapping algorithm to              |
| φ_diff(r_m | θ_diff^j) ≈ φ_test(r_m) − φ̂_test(r_m | θ̂^j),      |
+--------------------------------------------------------------+
                                  |
                                  v
+--------------------------------------------------------------+
| Obtain the ZF coefficient values of the unwrapping result,   |
| θ_diff^j, using the orthonormality of ZF polynomials.        |
+--------------------------------------------------------------+
                                  |
                                  v
+--------------------------------------------------------------+
| Update the ZF coefficients of the simulated test wavefront:  |
| θ̂^{j+1} = θ̂^j + θ_diff^j.                                     |
+--------------------------------------------------------------+
                                  |
                                  v
                  < Termination criteria < tolerance ? >  --- No, j=j+1
                                  |
                                 Yes
                                  v
                               ( End )
```
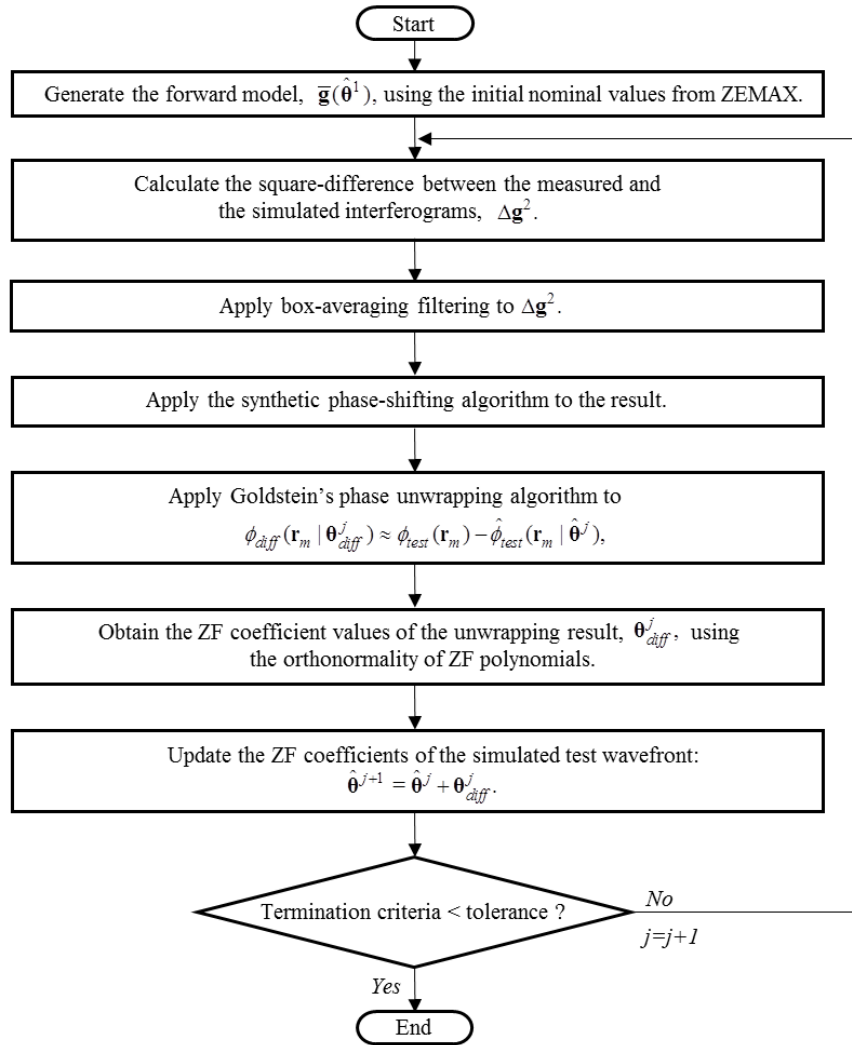
Fig. 4. The flow chart of the iterative synthetic phase-shifting algorithm. The box-averaging filtering process is optional for noise suppression, but it may improve the convergence rate.

3. Numerical studies

The SPS algorithm was verified with a series of computer simulation studies, and its application and performance was demonstrated. Since a monochromatic full-frame CCD (Kodak KAF-09000) was used for the prototype PDI, the fill factor of the CCD in the forward model was assumed to be 100% with a pixel size of 12μm$\times 12\mu$m. In order to represent the contiguous detector adequately, the simulation sub-pixelized the detector grid so that the resulting simulated interferogram did not suffer from aliasing. This super-sampled simulation was then down-sampled by averaging the sub-pixel values of each sub-pixelized block. The final sampling size of the simulated interferogram was equal to the detector size, 1024×1024 pixels. As shown in Appendix 7.1, the forward model is a mixture of the measured test beam

amplitude and an analytical function with 37 ZF coefficients. Due to the super-sampling requirement for the simulation, the test beam amplitude data were interpolated and a large matrix had to be calculated at each iteration. Therefore, the simulation was implemented using a parallel algorithm in the graphics processing unit (GPU) programming language, CUDA (Computer Unified Device Architecture). Particularly, we utilized the texture memory of the GPU to minimize the execution time for the test beam interpolation. A CUDA Cubic B-Spline Interpolation library implemented cubic interpolation using the texture memory [13]. The calculation time of the simulation (32768×32768 pixels) in double precision took 3.5 seconds using an NVIDIA Tesla C2075 card with 6 GB of on-board memory. The SPS algorithm was written in a combination of MATLAB®, C and CUDA, and a quad-core Intel Xeon 2.13 GHz processor was used. The model did not account for the effect of the micro lenses of the CCD.

To emulate the real experimental data, we first generated the simulated interferogram using the forward model and added zero-mean Gaussian noise with the measured noise variance of the CCD. After generating the data, we disregarded our knowledge of the true ZF coefficients, and estimated them by ML estimation using the SPS algorithm. The system construction parameters for the reference beam are d_{PDI}, C_{ref}, and $\mathbf{r}_c$, where d_{PDI} is the distance between the PDI plate to the detector plane, C_{ref} is the scalar amplitude of the reference beam, and $\mathbf{r}_c = (x_c, y_c)$ is the center position of the reference beam (Fig. 1 and Appendix 7.1). They were assumed to be known exactly in the numerical studies and the same experimentally measured test-beam amplitude was used in each of the simulations. The piston-corrected root-mean-square deviation (RMSD) between the measured and the simulated test wavefronts was chosen as a figure of merit for the numerical studies. It is denoted as

$$\sigma_{RMSD} = \sqrt{\frac{\sum_{m=1}^{M}\left[\phi_{test}(\mathbf{r}_m) - \hat{\phi}_{test}(\mathbf{r}_m)\right]^2}{M}}, \tag{10}$$

where m is the index of the CCD pixel and M is the total number of pixels within a circular aperture. In this study, the SPS algorithm was applied to interferograms whose spatial frequencies were lower and higher than the Nyquist condition.

3.1 An interferogram with a spatial frequency lower than the Nyquist condition

The first simulated noisy interferogram [Fig. 5(a)] was generated using the system construction parameter values (Table 1) and the true ZF coefficient values of the test wavefront (Table 2). The distance from the PDI plate to the CCD, d_{PDI}, was chosen such that the interferogram would satisfy the Nyquist condition. We then disregarded our knowledge of the true coefficient values, and estimated them by ML estimation using the iterative SPS algorithm. The initial values, $\hat{\boldsymbol{\theta}}^1$, and the final estimated results are shown in Table 2.

Table 1. The system construction parameter values for the reference beam at the detector plane used in Section 3.1. The values were chosen such that the departure of the test wavefront from the reference wavefront changes by less than half a wave over two adjacent pixels.

System Construction Parameter	d_{PDI}[mm]	x_c [mm]	y_c [mm]	C_{ref}[ADU$^{1/2}$]
Value	25.666	0.0	0.0	741

Table 2. The true ZF coefficients, the initial values and the final estimates of the test wavefront at the detector plane used in Subsection 3.1. The values of terms that are not listed are zero. All ZF coefficient values are in waves.

Index	Aberration Type	True	Initial	Estimate
2	Tilt x	0	1.2	0
3	Tilt y	0	-0.4	0
4	Defocus	592.7707	591.9707	592.7681
7	Coma x	0	0.3	0
8	Coma y	0	-0.5	0
9	Spherical Aberration, Primary	-32.9418	-32.5418	-32.932
16	Spherical Aberration, Secondary	5.4881	5.5681	5.4954
25	Spherical Aberration, Tertiary	-2.1501	-2.1501	-2.1605
36	Spherical Aberration, Quaternary	0.1490	0.1490	0.1338
37	Spherical Aberration, 12th- order term	-0.3450	-0.3450	-0.3373
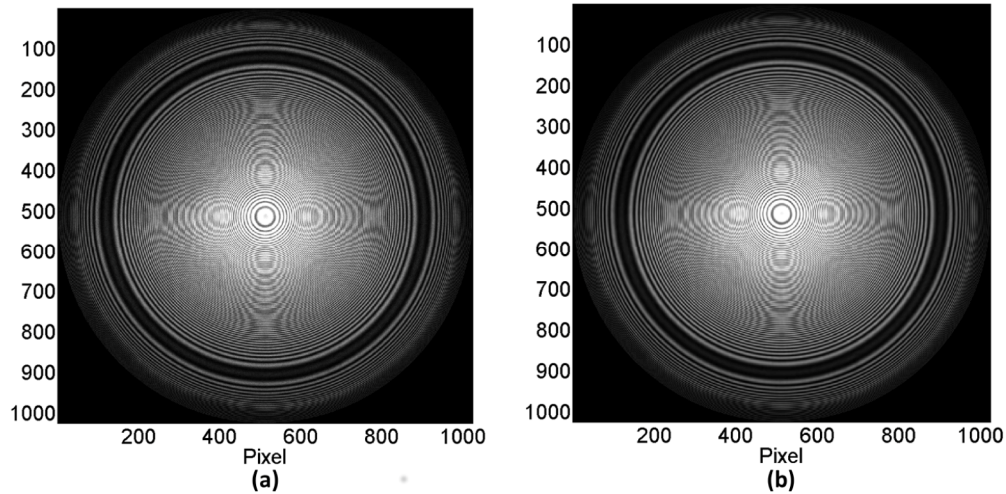
Fig. 5. (a) The first simulated noisy interferogram using the true values in Table 2 and (b) is the estimation result after 10 iterations of the SPS algorithm. Even though the spatial frequencies of the interferograms satisfy the Nyquist condition, some spurious fringes appear due to the aliasing by the monitor display sampling.

The piston-corrected RMSD converged to ~ 0.008 waves after 10 iterations of the SPS algorithm. The final estimated result is shown in Fig. 5(b).

3.2 An interferogram with a spatial frequency higher than the Nyquist condition

For the second numerical study, the noisy data were simulated using the system construction values in Table 3 and true parameter values in Table 4. All 37 true ZF coefficient values were chosen randomly from the initial values within a ±10 waves range. The local spatial frequency of the interferogram was higher than the Nyquist condition. After generating the noisy interferogram [Fig. 6(a)], we disregarded our knowledge of true ZF coefficient values and estimated them with the SPS algorithm. After 50 iterations, the estimated result [Fig. 6(b)] is compared to the noisy interferogram. A quantitative comparison between the true parameter values and their estimates is shown in Table 4 and the absolute differences between

two are shown in Fig. 7. Figure 8 shows a single profile of the true test wavefront and its estimated wavefront. The piston-corrected RMSD of the second simulated experimental data converged to ~ 0.009 waves after 50 iterations.

Table 3. The system construction parameters for the reference beam used in Subsection 3.2.

System Construction Parameter	d_{PDI} [mm]	x_c [mm]	y_c [mm]	C_{ref} [ADU$^{1/2}$]
Value	22.666	0.3854	-0.003	-741

Table 4. The true ZF coefficients and the initial values of the test wavefront used in Subsection 3.2. The estimation results are after 50 iterations of the SPS algorithm. All ZF coefficient values are in waves. The corresponding aberration types for some indices are shown in Table 2.

| Index	True	Initial	Estimate	Index	True	Initial	Estimate
2	-2.1123	0.0	-2.1120	20	2.1394	0.0	2.1311
3	5.662	0.0	5.660	21	-9.6740	0.0	-9.6731
4	598.7395	592.7707	598.7425	22	-5.1423	0.0	-5.1387
5	8.2324	0.0	8.2346	23	-7.2554	0.0	-7.2573
6	-6.0490	0.0	-6.0488	24	6.0835	0.0	6.0741
7	-3.2955	0.0	-3.2955	25	-9.0165	-2.1501	-9.0088
8	5.3646	0.0	5.3600	26	-1.9811	0.0	-1.9839
9	-37.3863	-32.9418	-37.3810	27	-7.4042	0.0	-7.4072
10	1.0794	0.0	1.0823	28	-7.8238	0.0	-7.8302
11	-0.4521	0.0	-0.4583	29	9.9785	0.0	9.9719
12	2.5774	0.0	2.5793	30	-5.6349	0.0	-5.6279
13	-2.7043	0.0	-2.7025	31	0.2586	0.0	0.2498
14	0.2680	0.0	0.2665	32	6.7822	0.0	6.7837
15	9.0466	0.0	9.0368	33	2.2528	0.0	2.2583
16	13.8120	5.4881	13.8185	34	-4.0794	0.0	-4.0811
17	2.7142	0.0	2.7093	35	2.7510	0.0	2.7420
18	4.3459	0.0	4.3407	36	0.6347	0.1490	0.6404
19	-7.1679	0.0	-7.1628	37	-0.4730	-0.3450	-0.4700
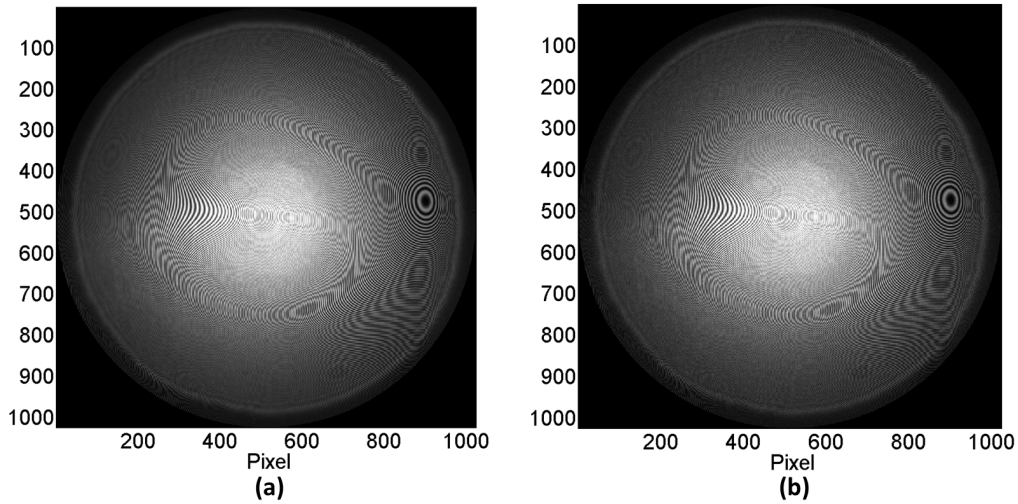
Fig. 6. (a) The simulated noisy interferogram was generated using the true values in Table 4 (Subsection 3.2) and (b) the estimated result after 50 iterations of the SPS algorithm. (Note: some spurious fringes may also be visible due to the aliasing by the monitor display sampling.)
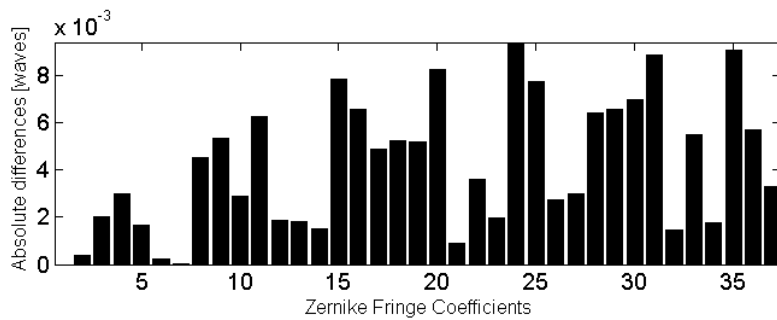

Fig. 7. The absolute differences (in waves) between the true ZF coefficients of the test wavefront used in Subsection 3.2 and their estimates after 50 iterations of the SPS algorithm.
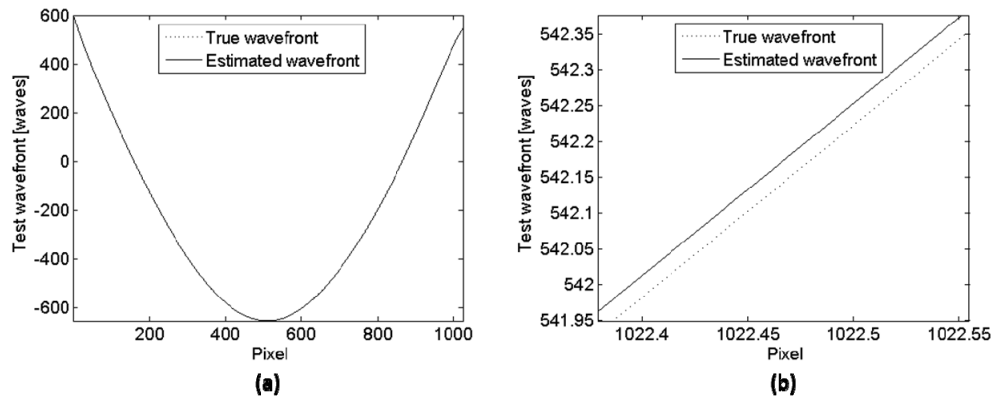

Fig. 8. (a) A single line profile of the true test wavefront used in Subsection 3.2 and its estimate after 50 iterations of the SPS algorithm. The true values and the estimates are almost overlapping each other. (b) The zoomed image of (a) at pixel 1022.

3.3 The convergence study

We performed two convergence studies in order to assess the robustness of the proposed algorithm. First, we simulated sensors with larger pixels to properly test the robustness of the SPS algorithm against a large wavefront deviation between two neighboring pixels. In other words, a different degree of pre-sampling low-pass filtering was introduced by increasing the size of a pixel by an integer multiple n. The output of a larger pixel was the average value of the corresponding $n \times n$ pixels of the finely-sampled detector ($12\mu m \times 12\mu m$ pixels). We used the noisy interferogram which satisfies the Nyquist condition (Subsection 3.1) as the outputs from the detector with the smallest pixel dimensions. Using the same true ZF coefficients in Table 2, we generated four different data sets depending on the different pixel sizes (Table 5 and Fig. 9). The corresponding piston-corrected RMSD of the test wavefront with different pixel sizes are shown in Table 5. It is important to note that the digitization error of a circular aperture contributes to the main piston-corrected RMSD errors for the larger pixel sizes.

Table 5. The piston-corrected RMSDs of the test wavefront at the detector plane with different pixel sizes. The true ZF coefficients of the test wavefront are shown in Table 2.

Pixel size [μm × μm]	12×12^{a}	24×24	48×48	96×96
Piston-corrected RMSD [waves]	~0.008	~0.008	~0.01	~0.04

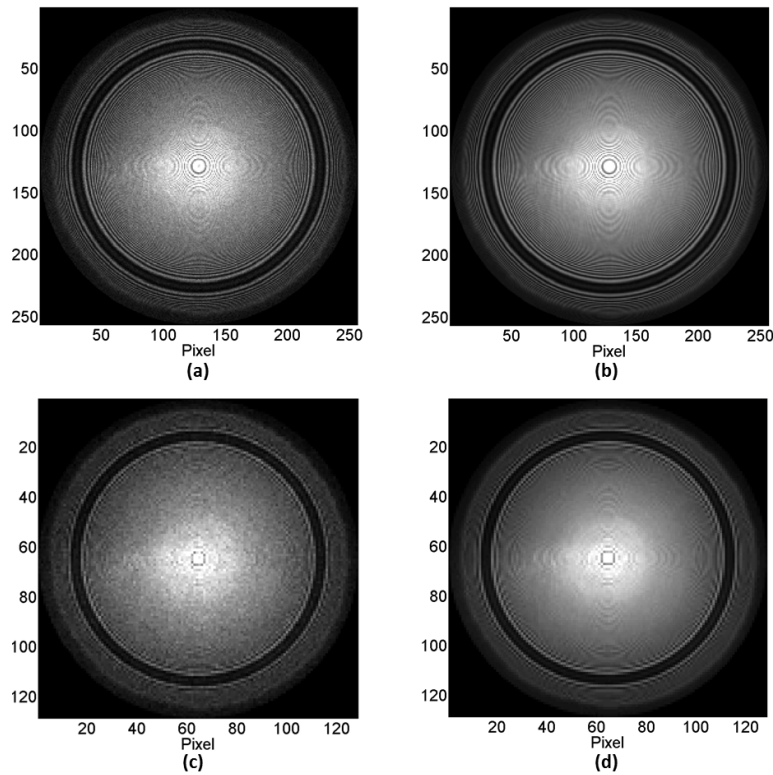[a]The spatial frequency of the interferogram satisfies the Nyquist condition.

Fig. 9. The simulated noisy interferograms using the true values in Table 2 with a pixel size of (a) $48\mu m \times 48\mu m$, and (c) $96\mu m \times 96\mu m$. (b) and (d) are the estimation results after the SPS algorithm was applied. (Note: some spurious fringes may also be visible due to the aliasing by the monitor display sampling).)
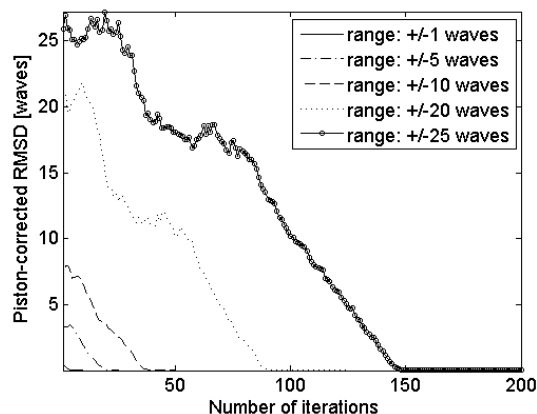
Fig. 10. The effect of different ranges of deviation between the initial values and the true values on the convergence to a threshold value.

Secondly, we tested the robustness of the algorithm against the deviation between initial values and the true ZF coefficient values. We varied the deviation range of the initial values from the true coefficient values at a fixed pixel size $(12\mu\text{m}\times12\mu\text{m})$. All 37 initial coefficient values of the test wavefront were randomly generated from the true values within ±1, ±5, ±10, ±20, and ±25 waves ranges. When the initial values were closer to the true values, the estimates converged to a threshold value with fewer iterations (Fig. 10). The threshold value (the piston-corrected RMSD) to terminate the iteration process for this study was 0.005 waves. Further optimization, such as post-filtering process, could improve the performance.

4. Experimental study

4.1 General design and layout

A proof-of-concept prototype PDI has been designed and built. The main configuration of our PDI was similar to a conventional PDI in a non-null configuration except that physical phase-shifters were not included (Fig. 11). An aspheric lens (Edmund optics 49104) with an entrance pupil diameter of 18 mm was tested for this study. According to Zemax, the exit pupil diameter and working f-number at the paraxial image location were $D_{\text{xp}} = 20.01$ mm and $\text{f}/\#_\text{W} = 2.537$, respectively. According to the manufacturer, the aspheric lens has ~1.25 waves RMS surface accuracy. The lens is designed to achieve a minimum aberration when the flat side of lens is facing the detector plane. However, in order to introduce a large aberration, the lens was flipped such that the flat side was facing the light source (Fig. 1). The exit pupil aberration of the lens in the flipped configuration was obtained using Zemax (Table 6).
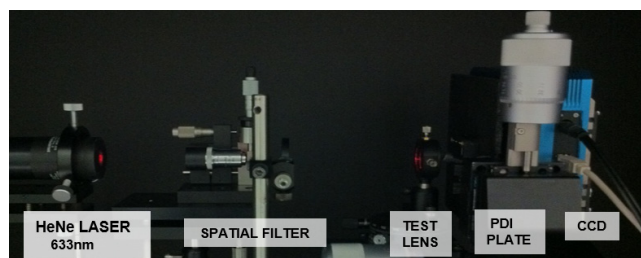

Fig. 11. The experimental setup of the prototype point-diffraction interferometer.

Table 6. ZF coefficients, peak-to-valley and RMS of the exit pupil aberration of the aspheric lens (Edmund 49104) obtained from Zemax. The center of the reference sphere is located at the paraxial image plane. The exit pupil diameter is 20.01 mm. The values of non-symmetric terms are zero.

Index	Aberration Type	Design Value
4	Defocus	43.7432894
9	Spherical Aberration, Primary	14.1472115
16	Spherical Aberration, Secondary	-0.2436503
25	Spherical Aberration, Tertiary	-0.0167761
36	Spherical Aberration, Quaternary	-0.0005934
37	Spherical Aberration, 12th- order term	-0.0000688
Peak-to-valley	N/A	86.9980866
RMS [waves]	N/A	25.7345771
Variance [waves^2]	N/A	662.2684598

The noisy data, g, consisted of the raw detector outputs from a CCD (Apogee Alta U9000) that measured the interference between the reference beam and the attenuated test beam at the detector plane. By translating the PDI plate in x, y and z directions, decenter and defocus were introduced in order to increase the fringe contrast. For the forward model, the amplitude function of the test beam was obtained experimentally via translation of the PDI plate such that the test beam does not pass through the pinhole but is attenuated by the PDI plate (Appendix 7.1). The scalar amplitude of the reference beam, C_{ref}, was calculated from the Michelson fringe contrast.

4.2 Point-diffraction interferometer plate

Different PDI schemes and PDI plate designs have previously been proposed, and much effort has been made to include phase-shifting techniques into PDI systems [14–18]. Instead of undertaking complicated fabrication processes, we used a simple PDI plate. It consists of a chromium layer deposited on a fused silica plate with a $R_{PDI} = 0.5\mu$m radius pinhole milled through the chromium layer by a focused ion-beam (FIB). The irradiance transmittance of the PDI plate was measured as ~0.0001%. Images of the pinhole, taken with a scanning electron microscope, are shown in Fig. 12.
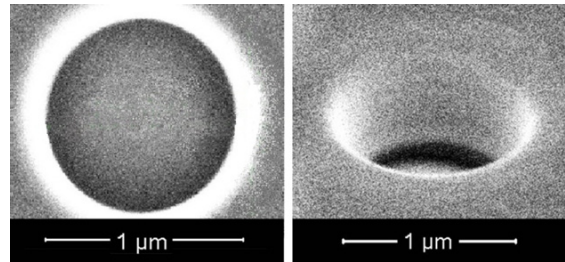

Fig. 12. The focused ion-beam etched pinhole on a chromium layer deposited on a fused silica plate. Images were taken with a scanning electron microscope.

4.3 Application of the synthetic phase-shifting algorithm

We applied the SPS algorithm to a measured interferogram acquired using the prototype PDI. The design values at the detector plane were obtained from the Zemax model of the PDI in the on-axis configuration (Table 7). Without knowledge of the true values, the design values

offered the best possible knowledge of the true values of the test lens. The measured system construction parameters (Table 8) were used for the reference beam. Unlike the numerical study, the true values were unknown for the physical data. Therefore, we set the termination criteria as the piston-corrected root-mean-square (RMS) of the $\phi_{diff}(\mathbf{r})$, denoted by

$$\sigma_{RMS} = \sqrt{\frac{\sum_{m=1}^{M}\left[\phi_{diff}(\mathbf{r}_m) - c_{diff}\right]^2}{M}}, \tag{11}$$

where m is the index of the CCD pixel, M is the total number of pixels within a circular aperture and c_{diff} is the piston term of $\phi_{diff}(\mathbf{r}_m)$. After 13 iterations, the piston-corrected RMS was ~0.006 waves, and the initial estimates of the test wavefront were obtained, including the alignment errors of the PDI system. Figure 13 shows the comparison between the measured and the estimated interferograms. The single line profiles through the measured and the estimated data in the x and y directions are compared in Fig. 14. Pearson's correlation coefficient between the measured data and the estimated data was ~0.95, indicating a high degree of correlation.

Table 7. The design ZF coefficient values at the detector plane obtained from Zemax. The final estimates were obtained after subtracting the alignment errors (tip/tilt and distances between the elements). The corresponding aberration types for some indices are shown in Table 2.

Index	Design[a]	Estimate	Index	Design[a]	Estimate
2	0	-0.763	20	0	-0.046
3	0	-0.278	21	0	0.104
4	565.495	565.802	22	0	0.053
5	0	0.321	23	0	-0.088
6	0	-0.290	24	0	-0.022
7	0	-0.167	25	-1.181	-1.186
8	0	-0.007	26	0	-0.111
9	-27.591	-26.098	27	0	-0.061
10	0	-0.044	28	0	0.107
11	0	-0.076	29	0	0.078
12	0	-0.047	30	0	-0.090
13	0	0.076	31	0	-0.041
14	0	-0.114	32	0	0.085
15	0	0.250	33	0	0.059
16	4.756	3.755	34	0	-0.071
17	0	0.049	35	0	0.096
18	0	0.070	36	0.3	0.351
19	0	-0.065	37	-0.121	-0.392

[a]The design values offered the best possible knowledge of the true values of the test lens.

Table 8. All system construction parameters were experimentally measured using a micrometer, except C_{ref} which was calculated by a local Michelson contrast measurement. The measurement error of d_{PDI} was large due to the limited access to the CCD plane.

System Construction Parameter	d_{PDI} [mm]	x_c [mm]	y_c [mm]	C_{ref} [ADU$^{1/2}$]
Value	23 ± 1	0.35 ± 0.05	0.0 ± 0.05	741 ± 20
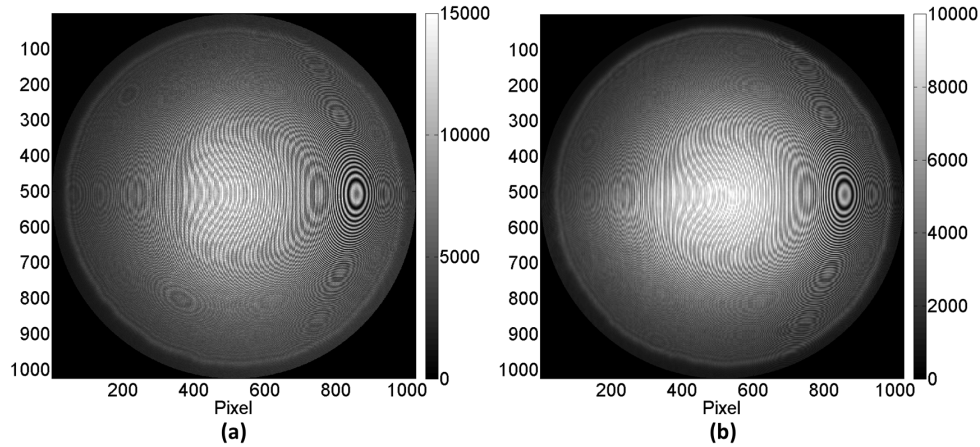
Fig. 13. (a) The measured interferogram obtained by using a f/#$_W$ = 2.537 aspheric lens. (b) The estimated interferogram after 13 iterations of the SPS algorithm. Pearson's correlation coefficient between the two images is ~0.95. (Note: some spurious fringes may also be visible due to the aliasing by the monitor display sampling.)
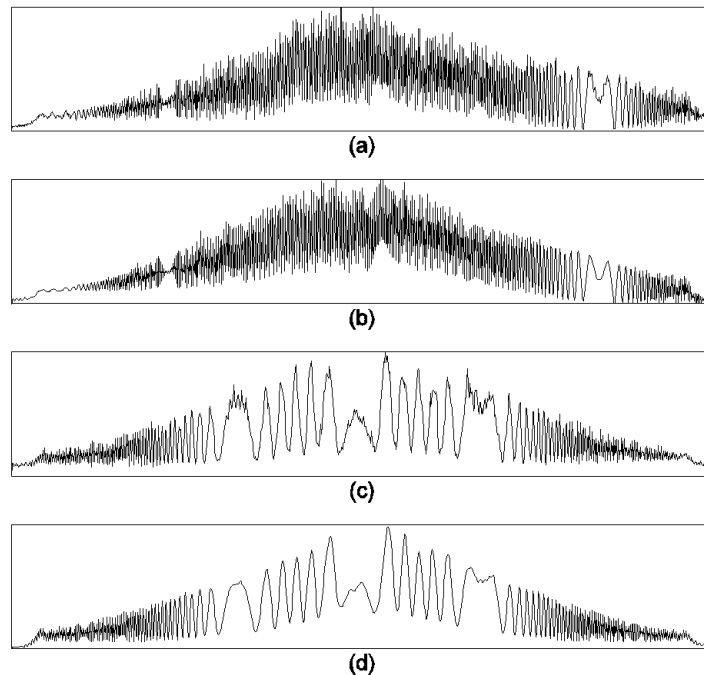

Fig. 14. A single line profile, through the x and y axes, comparison between the measured data [(a) and (c)] and the estimated results [(b) and (d)].

In order to obtain the final estimates of $\boldsymbol{\theta}$, we estimated alignment errors and subtracted them from the resulting ML estimates of the SPS algorithm. Using Zemax, alignment errors were obtained from a sensitivity analysis of the tilt angle of the optical elements and the spacing between the elements. The range of the tilt angle was $\pm 0.5\,^\circ$ and the range of the spacing between the elements was ± 0.5 mm. The ranges were within the alignment uncertainties of the prototype PDI. The final estimates, after subtracting the alignment errors, are compared with the design values in Table 7. The RMS difference error between the final estimated wavefront and the design wavefront was ~0.9 waves.

To compare this RMS difference error with the lens specification, we estimated root-sum-square (RSS) wavefront error (σ_{RSS}) of the test lens. The surface accuracy of the test lens (σ_{test}) was given as ~1.25 waves RMS from the lens specification (Subsection 4.1). From this RMS surface accuracy, the RSS value from the two uncorrelated surface errors was calculated by

$$\sigma_{RSS} = (n-1)(\sigma_{test}^2 + \sigma_{test}^2)^{1/2}, \tag{12}$$

where $n = 1.58$ was the index of refraction of the test lens. We obtained a RSS wavefront aberration of ~1.0 waves, which was comparable with the RMS difference error. An independent measurement of the test lens, using a null-testing setup, can be performed in future to validate our results.

5. Discussion

A question always arises about the sign ambiguity of Eq. (1) when a single-frame interferogram analysis method is proposed. For ML estimation of parameterized wavefronts, the sign ambiguity problem can be addressed in the following way: a ZF coefficient vector, $\boldsymbol{\theta}'$, always exists such that

$$\left[\sum_{p=1}^{P} \theta_p Z_p(\mathbf{r}) - \phi_{ref}(\mathbf{r}) \right] = -\left[\sum_{p=1}^{P} \theta_p' Z_p(\mathbf{r}) - \phi_{ref}(\mathbf{r}) \right], \tag{13}$$

where θ_p is the pth order ZF coefficient, and $Z_p(\mathbf{r})$ is the pth order ZF polynomial. Our approach can avoid this ambiguity if the distance between two parameter vectors, $\|\boldsymbol{\theta}' - \boldsymbol{\theta}\|$, which is derived from $\sum_{p=1}^{P}(\theta_p' - \theta_p)Z_p(\mathbf{r}) = -2\left[\sum_{p=1}^{P} \theta_p Z_p(\mathbf{r}) - \phi_{ref}(\mathbf{r}) \right]$, is larger than our prior knowledge of the search range of $\boldsymbol{\theta}$. In interferometry, we often have prior knowledge of the range of $\boldsymbol{\theta}$ within a few tens of waves. For example, the distance between the two parameter vectors, $\|\boldsymbol{\theta}' - \boldsymbol{\theta}\|$, in Subsection 3.2 is ~135 waves. Since the initial guess values for the SPS algorithm is much closer to the true ZF coefficient, $\boldsymbol{\theta}$, than $\|\boldsymbol{\theta}' - \boldsymbol{\theta}\|$, the resulting estimates can avoid the sign ambiguity.

Two limitations need to be addressed for this approach. First, we introduce a truncation error by truncating an infinite set of ZF polynomials to a finite set [6]. Therefore, it is impossible to fully determine a test wavefront even in the absence of noise. However, the number of parameters can be increased at a cost of increased computational time. The other error source is the accuracy of prior knowledge of the reference wavefront. We can reduce the error if the PDI system is carefully calibrated. For the calibration, another ML estimation can be also carried out for estimation of the system construction parameters [19]. If the exit pupil aberration of a test optic is the desired object wavefront, a reverse-ray tracing step can be added after estimating the wavefront at the detector plane.

6. Conclusion

In summary, using ML estimation with the novel SPS algorithm, a test wavefront, described by a finite set of ZF polynomials, was successfully estimated from a single interferogram from the PDI. The theory of the SPS algorithm and the forward model for the PDI have been established. The algorithm was verified with numerical and experimental studies using the PDI. The studies showed that the algorithm can recover the phase with a higher spatial frequency than the Nyquist frequency. The SPS algorithm can be used in a non-null configuration and does not require any physical phase shifters.

To conclude, the approach developed in this paper can provide an accurate tool for non-null testing with a high dynamic range in terms of measurable (i.e. estimable) test wavefront deviation from the reference wavefront. This high dynamic range enables its non-null testing capability for various optics including highly aspheric lenses and free-form optics and eliminates the complexity to build customized null configurations such as null-lens or computer generated holograms.

7. Appendix

7.1 Forward model for the point-diffraction interferometry

For the prototype PDI, the detector is directly located downstream from the PDI plate without relay optics. Therefore, the reference and the test wavefronts at the detector plane are the main interest of the forward model. Due to the simplicity of the system, the irradiance at the detector plane, $E(\mathbf{r} \mid \boldsymbol{\theta})$, can be written as follows

$$E(\mathbf{r} \mid \boldsymbol{\theta}) = \left| U_{test}(\mathbf{r}) + U_{ref}(\mathbf{r}) \right|^2, \tag{14}$$

where $U_{test}(\mathbf{r})$ and $U_{ref}(\mathbf{r})$ are the complex amplitudes of the test and the reference beams on the detector plane. It is explicitly shown as a function of the parameters of interest, the ZF coefficients. The complex amplitude of the test beam, $U_{test}(\mathbf{r})$, is expressed as

$$U_{test}(\mathbf{r}) = \alpha(\mathbf{r}) \exp\left[2\pi i \hat{\phi}_{test}(\mathbf{r}) \right], \tag{15}$$

where $\alpha(\mathbf{r})$ is the amplitude function, and $\hat{\phi}_{test}(\mathbf{r})$ is the test wavefront at the detector plane. It is denoted by

$$\hat{\phi}_{test}(\mathbf{r}) = \sum_{p=1}^{P} \theta_p Z_p(\mathbf{r}), \tag{16}$$

where $\mathbf{r} = (x, y)$ specifies the detector position over a circular aperture, $P = 37$, and θ_p is the pth component of $\boldsymbol{\theta}$, a 37×1 column vector of the ZF coefficients. It is assumed to be well approximated by a finite set of ZF polynomials, $\{Z(\mathbf{r})\}$. The amplitude function of the test beam $\alpha(\mathbf{r})$ is obtained experimentally via translation of the PDI plate such that the test beam does not pass through the pinhole but is attenuated by the PDI plate.

The complex amplitude of the reference beam, $U_{ref}(\mathbf{r})$, is assumed to have a spherical wavefront due to the small size ($\sim 1 \mu m$ diameter) of the PDI plate pinhole.

$$U_{ref}(\mathbf{r}) = \beta(\mathbf{r}) \exp\left(ik\sqrt{\left|\mathbf{r} - \mathbf{r}_c\right|^2 + d_{PDI}^2} \right) = \beta(\mathbf{r}) \exp\left[2\pi i \hat{\phi}_{ref}(\mathbf{r}) \right], \tag{17}$$

where $\beta(\mathbf{r})$ is the amplitude function, $k = 2\pi/\lambda$ is the angular wavenumber, d_{PDI} is the distance between the PDI plate to the detector plane, C_{ref} is the scalar amplitude of the reference beam, and $\mathbf{r}_c = (x_c, y_c)$ is the center position of the reference beam. The amplitude function of the reference beam is difficult to measure experimentally because it is impossible to mask PDI plate except a $\sim 1\mu m$ diameter pinhole. Since the pinhole of the PDI plate has a finite diameter, we assume that $\beta(\mathbf{r})$ is a result of the Fraunhofer diffraction without the paraxial approximation [6]. The final mean output from a CCD is an $M \times 1$ vector, $\overline{\mathbf{g}}(\boldsymbol{\theta})$, due to the mean irradiance, $\overline{E}(\mathbf{r} | \boldsymbol{\theta})$, incident on the detector. Its mth pixel CCD output (in unit of ADU) is denoted by

$$
\begin{aligned}
\overline{g}_m(\boldsymbol{\theta}) &\equiv R\overline{N}_m = R\eta T_{fr} \int_{A_m} \overline{E}(\mathbf{r} | \boldsymbol{\theta}) d\mathbf{r} \\
&= R\eta T_{fr} \int_{A_m} \left(\alpha(\mathbf{r})^2 + \beta(\mathbf{r})^2 + 2\alpha(\mathbf{r})\beta(\mathbf{r}) \cos\left\{ 2\pi \left[\hat{\phi}_{test}(\mathbf{r} | \boldsymbol{\theta}) - \hat{\phi}_{ref}(\mathbf{r}) \right] \right\} \right) d\mathbf{r},
\end{aligned}
\tag{18}
$$

where R is the responsivity of the mth pixel and its unit is analog-to-digital units (ADU) per photoelectron. The mean number of photoelectrons generated in the mth pixel is $\overline{N}_m$, the quantum efficiency is η in units of photoelectrons/joule(J), the area of the mth pixel is A_m, and T_{fr} is the frame-acquisition time. In this work, all pixels are assumed to have the same responsivity and quantum efficiency. For simplicity, Eq. (18) is rewritten as

$$
\overline{g}_m(\boldsymbol{\theta}) = \int_{A_m} \left\{ \hat{B}(\mathbf{r}) + \hat{\gamma}(\mathbf{r}) \cos\left[2\pi\phi_{sim}(\mathbf{r} | \boldsymbol{\theta}) \right] \right\} d\mathbf{r},
\tag{19}
$$

where $\phi_{sim}(\mathbf{r} | \boldsymbol{\theta}) = \hat{\phi}_{test}(\mathbf{r} | \boldsymbol{\theta}) - \hat{\phi}_{ref}(\mathbf{r})$ is the simulated wavefront difference between the reference and the test wavefronts.

7.2 The derivation of the squared difference between the measured and simulated CCD outputs

The measured CCD output in the mth pixel from the PDI with noise, is given by

$$
g_m = \int_{A_m} \left\{ B(\mathbf{r}) + \gamma(\mathbf{r}) \cos\left[2\pi\phi_{exp}(\mathbf{r}) \right] \right\} d\mathbf{r} + n_m,
\tag{20}
$$

where $B(\mathbf{r})$ and $\gamma(\mathbf{r})$ are the physical quantities corresponding to $\hat{B}(\mathbf{r})$ and $\hat{\gamma}(\mathbf{r})$ in Eq. (19). The true wavefront deviation between a reference and a test wavefront is $\phi_{exp}(\mathbf{r}) = \phi_{test}(\mathbf{r}) - \phi_{ref}(\mathbf{r})$, and n_m is additive zero-mean Gaussian noise in the mth pixel.

The SPS algorithm minimizes the squared difference between the measured and the simulated CCD outputs, which is an $M \times 1$ vector, denoted $\Delta \mathrm{g}^2$, with its mth component given by

$$
\Delta g_m^2 \equiv [g_m - \overline{g}_m(\boldsymbol{\theta})]^2.
\tag{21}
$$

If we assume that the measured and the simulated mean irradiances are approximately the same, so that $\gamma(\mathbf{r}) \cong \hat{\gamma}(\mathbf{r})$,

$$
\Delta g_m^{\ 2} \approx \left[\int_{A_m} \left(\gamma(\mathbf{r}) \left\{ \cos\left[2\pi\phi_{exp}(\mathbf{r}) \right] - \cos\left[2\pi\phi_{sim}(\mathbf{r}) \right] \right\} + B(\mathbf{r}) - \hat{B}(\mathbf{r}) \right) d\mathbf{r} + n_m \right]^2.
\tag{22}
$$

By using a simple trigonometric identity, Eq. (22) can be rewritten as

$$\Delta g_m^{\ 2} \approx \left(\begin{array}{l} \int_{A_m} 2\gamma(\mathbf{r}) \sin\left\{ \pi \left[\phi_{exp}(\mathbf{r}) - \phi_{sim}(\mathbf{r}) \right] \right\} \sin\left\{ \pi \left[\phi_{exp}(\mathbf{r}) + \phi_{sim}(\mathbf{r}) \right] \right\} d\mathbf{r} \\ + \int_{A_m} \left[B(\mathbf{r}) - \hat{B}(\mathbf{r}) \right] d\mathbf{r} + n_m \end{array} \right)^2 . \quad (23)$$

We define the phase difference of the true wavefront deviation and the simulated wavefront deviation as $\phi_{diff}(\mathbf{r}) = \phi_{exp}(\mathbf{r}) - \phi_{sim}(\mathbf{r}) = \left[\phi_{test}(\mathbf{r}) - \phi_{ref}(\mathbf{r}) \right] - \left[\hat{\phi}_{test}(\mathbf{r} \mid \boldsymbol{\theta}) - \hat{\phi}_{ref}(\mathbf{r}) \right]$. The first assumption occurs when the spatial fringe period of $\phi_{diff}(\mathbf{r})$ is very large compared to a CCD pixel [Figs. 2(f)–2(i)]; the spatial fringe period gets larger as the simulated wavefront deviation gets closer to the true wavefront deviation. In this case, the irradiance fluctuation due to $\phi_{diff}(\mathbf{r})$ is constant over a pixel. Therefore, irradiance fluctuation by $\phi_{diff}(\mathbf{r})$ can be merely sampled at the center position of a CCD pixel instead of integrating over the pixel. On the other hand, the spatial fringe period of $\phi_{sum}(\mathbf{r}) = \phi_{exp}(\mathbf{r}) + \phi_{sim}(\mathbf{r})$ should be well beyond the Nyquist condition, so the irradiance fluctuation due to $\phi_{sum}(\mathbf{r})$ is blurred out by the integration. Therefore, $\Delta g_m^{\ 2}$ becomes

$$\Delta g_m^{\ 2} \approx \left(B_m' + \gamma_m' \sin\left[\pi \phi_{diff}(\mathbf{r}_m) \right] \right)^2 , \quad (24)$$

where $\mathbf{r}_m$ is the center position of the mth pixel of the CCD, and B_m' is given by

$$B_m' \equiv \int_{A_m} \left\{ B(\mathbf{r}) - \hat{B}(\mathbf{r}) \right\} d\mathbf{r} + n_m . \quad (25)$$

The integration of the fast irradiance fluctuation over a pixel is denoted by

$$\gamma_m' \equiv \int_{A_m} \left\{ 2\gamma(\mathbf{r}) \sin\left[\pi \phi_{sum}(\mathbf{r}) \right] \right\} d\mathbf{r} . \quad (26)$$

This integration acts as a pre-sampling low-pass filter on $\Delta g_m^{\ 2}$. By applying a trigonometric identity to Eq. (24), the final expression for $\Delta g_m^{\ 2}$ is given by

$$\Delta g_m^{\ 2} \approx B_m'' + \gamma_m'' \cos\left[2\pi \phi_{diff}(\mathbf{r}_m) \right], \quad (27)$$

where $\gamma_m'' = -\gamma_m'^{\ 2}/2$, and $B_m'' = B_m'^{\ 2} + \gamma_m'^{\ 2}/2 + 2\gamma_m' B_m' \sin\left[\pi \phi_{diff}(\mathbf{r}_m) \right]$. Although B_m'' shows a slower spatial frequency, the dominant spatial frequency term in Eq. (27) is $\phi_{diff}(\mathbf{r}_m)$ if the mean signal, γ_m', is much larger than noise term, B_m'. From Eq. (27), we can treat Δg^2 as an interferogram which shows the phase difference, $\phi_{diff}(\mathbf{r})$. We can further suppress the noise of the final map of Δg^2 by applying a low-pass filter such as a box-averaging filter. Even though this filtering process is optional, it may improve the convergence rate. Further study is required to optimize the filtering process.

Acknowledgments